Detection, analysis and removal of glitches from InSight's seismic data from Mars

John-Robert Scholz[1], Rudolf Widmer-Schnidrig[2], Paul Davis[3], Philippe Lognonné[4], Baptiste Pinot[5], Raphaël F. Garcia[5], Francis Nimmo[6], Kenneth Hurst[7], Salma Barkaoui[4], Sébastien de Raucourt[4], Laurent Pou[6], Guénolé Mainsant[5], Nicolas Compaire[5], Arthur Cuvier[8], Éric Beucler[8], Mickaël Bonnin[8], Rakshit Joshi[1], Eléonore Stutzmann[4], Martin Schimmel[9], Anna Horleston[10], Maren Böse[11], Savas Ceylan[13], John Clinton[11], Martin van Driel[13], Taichi Kawamura[4], Amir Khan[12,13], Simon C. Stähler[13], Domenico Giardini[13], Constantinos Charalambous[14], Alexander E. Stott[14], William T. Pike[14], Ulrich R. Christensen[1], W. Bruce Banerdt[7]

[1]Max Planck Institute for Solar System Research, Justus-von-Liebig-Weg 3, 37077 Göttingen, Germany
[2]Black Forest Observatory, Institute of Geodesy, Stuttgart University, Heubach 206, D-77709 Wolfach, Germany
[3]Department of Earth, Planetary, and Space Sciences, University of California Los Angeles, CA90095, USA
[4]Université de Paris, Institut de physique du globe de Paris, CNRS, F-75005 Paris, France
[5]Institut Supérieur de l'Aéronautique et de l'Espace SUPAERO, 10 Avenue Edouard Belin, 31400 Toulouse, France
[6]Dept. of Earth and Planetary Sciences, University of California Santa Cruz, Santa Cruz, CA 95064, USA
[7]Jet Propulsion Laboratory, California Institute of Technology, Pasadena, CA 91109, USA
[8]Laboratoire de planétologie et géodynamique, CNRS UMR 6112, Université de Nantes, Université d'Angers, France
[9]Institute of Earth Sciences Jaume Almera – CSIC, Barcelona, Spain
[10]School of Earth Sciences, University of Bristol, Wills Memorial Building, Queens Road, Bristol BS8 1RJ, UK
[11]Swiss Seismological Service (SED), ETH Zurich, Sonneggstr. 5, 8092 Zurich, Switzerland
[12]Institute of Theoretical Physics, University of Zurich, Zurich, Switzerland
[13]Institute of Geophysics, ETH Zürich, Sonneggstrasse 5, 8092 Zürich, Switzerland
[14]Department of Electrical and Electronic Engineering, Imperial College London, South Kensington Campus, London, SW7 2AZ, United Kingdom

Key Points:

- Glitches represent small steps in the recorded acceleration
- Glitches are mostly due to relaxations of thermal stresses and instrument tilt
- We provide a toolbox to automatically detect and remove glitches

Corresponding author: John-Robert Scholz, `scholz@mps.mpg.de`

Abstract

The SEIS instrument package with the three very broad-band and three short period seismic sensors is installed on the surface on Mars as part of NASA's InSight Discovery mission. When compared to terrestrial installations, SEIS is deployed in a very harsh wind and temperature environment that leads to inevitable degradation for the quality of the recorded data. One ubiquitous artifact in the raw data is an abundance of transient one-sided pulses often accompanied by high-frequency precursors. These pulses, which we term "glitches", can be modeled as the response of the instrument to a step in acceleration, while the precursors can be modeled as the response to a simultaneous step in displacement. We attribute the glitches primarily to SEIS-internal stress relaxations caused by the large temperature variations to which the instrument is exposed during a Martian day. Only a small fraction of glitches correspond to a motion of the SEIS package as a whole and they are all due to minuscule instrument tilts. In this study, we focus on the analysis of the glitch+precursor phenomenon and present how these signals can be automatically detected and removed from SEIS' raw data. As glitches affect many standard seismological analysis methods such as receiver functions or spectral decomposition, we anticipate that studies of the Martian seismicity as well as studies of Mars' internal structure should benefit from deglitched seismic data.

Plain Language Summary

The SEIS instrument package with two fully equipped seismometers is installed on the surface of Mars as part of NASA's InSight Discovery mission. When compared to terrestrial installations, SEIS is more exposed to wind and daily temperature changes that leads to inevitable degradation in the quality of the recorded data. One consequence is the occurrence of a specific type of transient noise that we term "glitch". Glitches show up in the recorded data as one-sided pulses and have strong implications for the typical seismic data analysis. Glitches can be understood as step-like changes in the acceleration sensed by the seismometers. We attribute them primarily to SEIS-internal stress relaxations caused by the large temperature variations to which the instrument is exposed during a Martian day. Only a small fraction of glitches correspond to a motion of the whole SEIS instrument and they are all due to minuscule instrument tilts. In this study, we focus on the detection and removal of glitches and anticipate that studies of the Martian seismicity as well as studies of Mars' internal structure should benefit from deglitched seismic data.

1 Introduction

InSight (Interior Exploration using Seismic Investigations, Geodesy and Heat Transport) landed successfully on Mars on November 26, 2018 (Sol 0, a sol is a Martian day with around 24h 40m). Since February 9, 2019 (Sol 73), InSight's main scientific instrument SEIS (Seismic Experiment for Internal Structure) is recording seismic data in its operational configuration (Banerdt et al., 2020). The SEIS package (Lognonné et al., 2019), whose network and station code for the scientific data is XB.ELYSE, consists of two three-component seismometers; one being very broadband (VBB) with a corner period of 16 seconds, and one being short-period (SP) with a corner period of 35 seconds. Notwithstanding the corner periods, the noise floor of the two instruments is equivalent only above 4 Hz while it is about ∼30 dB lower for the VBB at frequencies of 0.1 Hz and less. The VBB is therefore the main instrument to detect distant Marsquakes, while the SP is used to cover the frequency range of ∼5–50 Hz for more detailed analysis of regional events and lander-induced signals. Both seismometers have non-orthogonal sensor orientations (Fig. 1a,c). To date, all six seismic components as well as the acquisition system have functioned nominally, exceeded mission requirements, and delivered unprecedented seismic data from the surface of Mars (InSight Mars SEIS Data Service, 2019). In addition to seismic signals of natural and artificial origins, i.e. Marsquakes (Lognonné et al., 2020; Giardini et al., 2020; for Marsquake catalog see: InSight Marsquake Service, 2020) and records from the HP^3-instrument hammering sessions (Spohn et al., 2018), respectively, these data show a variety of non-seismic signals whose origin is not always clear but under investigation. Amongst the most prominent and abundant types of these non-seismic signals are what we termed a "glitch". Glitches influence many of the standard seismological methods such as receiver functions, polarization analyses and spectral decomposition and hence their correct treatment is of high importance. The present study focuses on the detection, analysis and removal of glitches and extends Supplement V of Lognonné et al. (2020).

Glitches

A glitch (Fig. 1b,d) is a particular type of transient instrumental self-noise that, in the raw time series data, appear as a high amplitude, one-sided pulse with a duration controlled by the respective seismometer's transfer function. For the VBB sensors, which have 76% of critical damping, glitches have a fast rise time followed by an exponential decay with a small (∼9%) overshoot before, almost, returning to the baseline after ∼25 s. For the SP sensors, that are overdamped with 110% of critical damping, glitches have a similar rise time followed by a decay that takes the form of a near critically damped sinusoidal before, almost, returning to the baseline after ∼40 s. Glitches may also occur before a previous glitch has sufficiently decayed. The highest order of such "poly-glitches" we observe to date is four. Glitches (and poly-glitches) can occur on all three VBB and all three SP sensors simultaneously but there are many examples where a glitch occurs on only one component. They occur at all times of the sol but are observed more frequently during the quiet parts in the early evening and night (Fig. 2a). This is due the decreased seismic noise level driven by diurnal wind and pressure variations. The largest glitches reach amplitudes of $1e^{-7}ms^{-1}$ and more. We observe a few of these per sol, whilst for amplitudes of $\sim 1e^{-8}ms^{-1}$ we can observe already hundreds per sol. Especially in the early evening, when the wind and pressure variations calmed, we observe a period with many consecutive glitches mostly of lower amplitude (Fig. 2b). Certain types of glitches can furthermore repeat over many consecutive sols and the same local time, thus indicating a driving process behind their generation. In the frequency domain, glitches range from lowest frequencies up to almost 1 Hz, thus influencing analyses of seismic records, especially for longer periods. If glitches can be modeled with a step in acceleration, which is the working hypothesis of this study, then their spectrum is $1/f$ multiplied by the instrument response.

Glitch Precursors

Many glitches, furthermore, show a high-frequency signal at their very glitch beginning which lasts ∼2 s. We refer to these initial oscillations as "glitch precursors". These precursors occur simultaneously with the glitch onset for both VBB and SP (Fig. 1b,d). Glitch precursors do not represent artifacts caused by the on-board data decimation but instead, as we demonstrate, can be modeled as a response to a step in displacement. To facilitate the analysis of glitches and help deciphering their origins, we analyse these precursors as well.

2 Glitch Detection

To automatically detect glitches on SEIS' VBB and SP raw data, several groups (MPS, ISAE, UCLA, IPGP) independently developed algorithms in the Python and MATLAB programming languages. We describe these approaches in the following. The common detection idea, and working hypothesis of this study, is that glitches in the raw data represent steps in acceleration convolved with the seismometer's instrument response. The lists of detected glitches in 2019 can be found in the Supplementary Information 1.

2.1 Glitch Detection by Instrument Response Deconvolution (MPS)

This detection algorithm, implemented in Python (Rossum, 1995) and ObsPy (Krischer et al., 2015; Beyreuther et al., 2010), performs the following processing steps on a given period of three-component seismic data (components U, V, W): (i) ensure all three seismic channels are present and cut to equal length, i.e. handle gaps and overlaps, (ii) decimate the data to two samples per second (sps), allowing all data per seismometer to be run with the same parameters, (iii) deconvolve the instrument response on each component and convert to acceleration, (iv) band-pass filter the acceleration data (e.g. 10-1000 s, 0.001-0.1 Hz), so the steps in acceleration emerge more clearly, (v) calculate the time derivative of the filtered acceleration data so the acceleration steps become impulse-like signals, and (vi) trigger positive and negative glitches when the absolute value of the time-derivative of the filtered acceleration exceeds a constant. To avoid triggering on subsequent samples also exceeding the threshold but belonging to the same glitch, we introduce a window length in which no further glitch can be triggered. This parameter can be thought of as *minimum glitch length*. We note this parameter is smaller than the typical glitch length for VBB and SP, allowing our detection algorithm to detect poly-glitches.

The above processing results in a list of glitch start times for each of the individual UVW-components. A glitch simultaneously occurring on multiple components is detected on each affected component but the respective start times may slightly differ. However, after modeling of the full glitch waveform (Section 4) we can retrospectively establish that such glitches occur at the same time to within milliseconds. This holds true for all multi-component glitches observed to date on either VBB or SP, also for data with the highest available sampling frequency of 100 Hz. Therefore, we unify the individual glitch start times across the UVW-components by searching for all glitch starts within the minimum glitch length and use the earliest as the actual glitch start time. This unified list of glitch starts contains still many false-positive triggers caused by non-glitches with a steep enough acceleration change to be triggered. This is because we choose to apply a constant threshold to the time derivative of the filtered acceleration, rather than a threshold based on the current seismic noise level that undergoes glaring diurnal changes dominated by meteorological influences (e.g. Banfield et al., 2020). To circumvent this we rotate the gain-corrected UVW raw data of the glitch windows into the geographical reference frame (ZNE-components) and perform a 3-D principle component analysis (e.g. Scholz et al., 2017). Theoretically a glitch is linearly polarized as the associated vector of acceleration change is not varying. This linear polarization can only be slightly reduced by seismic noise. Indeed, we find most glitches exhibit a high linear polarization >0.9, a fact that we use to discriminate against other triggered signals. The polarization analysis further allows to obtain the apparent glitch azimuth and incidence angle which can be used to associate glitches with a particular glitch source (Section 3). Visual inspection reveals the resulting glitch onsets are usually accurate to within ± 1 s (e.g. green lines in Fig. 1b,d). We note that scheduled movements of InSight's robotic arm may be identified as glitches, however, these movement times are known and occur during the Martian daytime when we detect relatively few glitches. At times we also detect convective vortices (e.g. Banfield et al., 2020) as they can produce glitch-like signals in the seismic data (Section 6.3).

2.2 Glitch Detection by Cross-Correlation with Impulse Response Function (ISAE)

The principle of this MATLAB-implemented detection algorithm is cross-correlation. It performs the following processing steps on a given period of three-component raw seismic data (components U, V, W): (i) a synthetic glitch is constructed by convolving the poles and zeros of the transfer function of the VBB and SP sensors with a step in acceleration. To increase the temporal resolution to sub-sample range, we synthesise several glitches each with a different sub-sample time shift, (ii) the long period variations of the data are extracted using a 1000 s low-pass filter for VBB and a 4000 s low-pass filter for SP. These are then subtracted from the signal (and added back at the end), before (iii) the synthetic glitch is cross-correlated with the data. A glitch detection is triggered for the maxima of the cross-correlation function that exceed a threshold a on a given component.

Another step is added to prevent non-detection of glitches or false-positives, depending on the correlation threshold. For that, two thresholds are chosen: *threshold a* and *threshold b*, with $a \geq b$. The first step presented above is done for each component, with *threshold a*. Then, for each component, a second cross-correlation with *threshold b* is implemented. For the times of every maximum of cross-correlation exceeding *threshold b*, we come back to the glitches detected on the other components during the first step. If a glitch had indeed been detected at that specific time on another component, a new glitch is declared on the component under study. We can therefore detect small glitches with low signal-to-noise ratio when a strong glitch is detected at the same time on some other component. In addition, in order to be able to detect poly-glitches, a second iteration of the detection algorithm is performed after the glitches from the first iteration have been removed from the data.

2.3 Hierarchical Glitch Detection (UCLA)

This MATLAB based method took into account that glitch amplitudes follow a power law distribution with many more very small glitches than larger ones. Therefore the strategy was to remove the largest glitches first and repeat the process on the smaller ones in an iterative procedure. In this method the raw UVW VEL channel data are inspected for glitches and their precursors. The instrument response to a step in acceleration was termed "Green's function." The 20 sps data were decimated to 2 sps and each channel was tested for correlation with the response function as follows. An inverse filter was designed that turned glitches into Gaussians so that each glitch represented one peak without the overshoot. An STA/LTA (short time average / long time average) ratio was found using convolution of the data with box car functions. The absolute value of band-passed data was

tested for peaks above the STA/LTA threshold. For the first iteration the STA/LTA was set large to remove the largest glitches. The Green function was correlated with the data spanning a peak and if the correlation coefficient was above 0.95 the detection was registered. If multiple peaks occurred close together, multiple Green's functions were fit to the data using nonlinear least squares. The data was then cleaned by removing the glitches. The process was then repeated lowering the STA/LTA threshold=7, and the new glitches removed from the data. For the last iteration the STA/LTA threshold was set to 3, i.e. lowered again and the correlation threshold was also lowered to 0.8. This removed many of the small glitches. Our glitch detection is applicable to SEIS' VBB and SP sensors in both low and high gain modes.

2.4 Triple-Source based Glitch Detection (IPGP)

Implemented in MATLAB, this glitch detection method processes mostly 2 sps continuous data and is therefore focused on long period continuous signals. It first removes the aseismic signals of each raw axis by subtracting the trend and the first 12 sol-harmonics (i.e., up to 1/12 sol period, about 0.13 mHz in frequency). Then the three axes are equalized in digital units by convolving the V and W channels by the convolution ratio of the U/V and U/W transfer functions, in order to correct for the gain and transfer function differences between U, V and W. Note that this process also transforms an impulse response in time on V and W into an impulse response with the U transfer function. As the inversion (below) is a linear one, the glitch search and deglitching can be done either on the UVW or on the ZNE rotated channels, with practically no differences for the inverted glitches.

The glitch detection is done first by identifying all extrema in the signal and then, for all found extrema, least-square testing for the occurrence of a glitch using a modeled glitch. To model a glitch, we convolve a step in acceleration not only for one sample (as all other methods) but for three consecutive samples. As we have equalized all components beforehand, we only use the poles and zeros of the U-component for this step. Continuity of the signal is forced at the beginning and at the end of the glitch window by Lagrangian multipliers (Lagrange, 1813). The signal is then considered a glitch when the variance residual after glitch removal is less than 1–2 % of the original data squared energy over a running window of 50 s, starting 5 s before the glitch center. To remove the glitch precursors after the glitch removal, a delta impulse is then searched around the glitch time and removed if associated with a 50 % variance reduction of the signal in a window of width ± 3 s. Glitches and precursor amplitudes are inverted on the three axes. We use these amplitudes to calculate dip, azimuth and amplitudes of the precursors that we use to potentially located glitch source (Section 6.1). An average of about 170 glitches per sol is found for 1 % of variance residual and about 100 glitches per sol for 0.5 % of variance residual. For the former case, about 40 % are detected on the three components while the other are on single VBB components. As this approach is detecting the glitch through the success of the functions' fit with data, glitch removal is a sub-product of the method.

2.5 Performance of Glitch Detection Algorithms

A 24 hours comparison of our glitch detection algorithms is illustrated Figure 2. The detection threshold for some methods was set low in order to examine differences in the detections close to the ambient seismic noise levels. For example, ISAE and UCLA used a correlation coefficient threshold of 0.8 which opens the possibility that some of the detections may be noise. Approximately 250 detections were made by UCLA and IPGP, and 140 by MPS and ISAE, however, the latter two detected less glitches during the noise daytime. Figure 2a shows the 73 glitches that were common to all 4 groups, which correspond to those with the largest amplitude. Table 1 shows the number of detected glitches common to pairs of groups. The non-common glitches are plotted color-coded according to each group. A zoomed-in section (Fig. 2b) reveals that the various criteria detect mutually exclusive glitches as the noise level is approached. We note that the MarsQuakeService (MQS, Clinton et al., 2018) continuously monitors InSight's seismic data to detect and catalogue seismic events (InSight Marsquake Service, 2020). As part of their routine they manually seek and annotate glitches with principal focus on time windows of seismic events. Our detection methods generally compare well with these manual annotations both in amount and onsets of glitches, especially for larger ones.

Table 1. Common glitch detections between group pairs for July 1 2019, sol 211. Based on data of 02.BHV (VBB at 20 sps). Note that all algorithms equally detect the largest 73 glitches.

GROUP	MPS	ISAE	IPGP
ISAE	94		
IPGP	102	95	
UCLA	105	100	121

3 Glitch Analysis

Our working hypothesis is that glitches in SEIS' time series data represent sudden steps in the sensed acceleration convolved with the instrument response of the respective seismometer, either VBB or SP. We can use that assumption to constrain the physical mechanism that led to the glitch. When interpreted as an inertial acceleration of the seismometer frame, a step in acceleration translates to a unlimited linear increase of velocity. This of course becomes quickly non-physical and can be ruled out because it implied that SEIS by now would have left its landing location. On the other hand, accelerometers like the VBB or SP are also sensitive to changes in gravity. One way this can occur is by tilting the instrument, thus causing a change of projection of the local gravity vector onto the directions of the sensitive sensor axes. For small tilt angles α, this translates into a first order effect for the horizontal components ($\sim\sin(\alpha) \approx \alpha$) but only a second order effect for the vertical component ($\sim [1 - \cos(\alpha)] \approx \alpha^2/2$). The vector sum of acceleration changes in U, V and W due to a tilt of the SEIS sensor assembly (including the leveling system) must therefore point in the horizontal direction. This is true for both SP and VBB. Any other direction cannot be explained by a rigid motion of SEIS and must be due to instrumental artifacts.

It is useful to recall the sign convention for accelerometers: a positive output signal corresponds to a positive acceleration of the frame in the sensitive direction, not the direction in which the proof mass moved. The proof mass – due to its inertia – lags behind the motion of the frame. Therefore, if one analyses the apparent glitch azimuth and incidence angles under consideration of the actual sensor orientations as well as the behaviour of these angles over time, one can draw conclusions on possible glitch origins. The analysis of apparent glitch polarizations is therefore our method of choice.

The determination of the apparent glitch azimuth and incidence angles is implemented in our glitch detection algorithm (Section 2.1). As described, once a glitch onset is detected, the algorithm divides the raw data by the respective sensor gains, rotates the data into the geographical reference frame (ZNE-components) and performs a 3-D principle component analysis (e.g. Scholz et al., 2017). To resolve the 180° ambiguity inherent to that method, we used the fact that glitches have a clear one-sided pulse (1b,d); a glitch of positive polarity on the N-component is associated with a step in acceleration acting in this direction, its respective azimuth is therefore ≈0° (assuming there is no glitch on the E-component). The same consideration holds true for a glitch showing on the (reconstructed) vertical component.

Figures 3–5 demonstrate the polarization analysis of the VBB and SP glitches for 2019. The plots incorporate two VBB channels 02.BH? and 03.BH? (20 sps and 10 sps, respectively), and two SP channels 67.SH? and 68.SH? (20 sps and 10 sps sample rate, respectively). These are the channels that, depending on the actual satellite down-link capacities, are continuously returned to earth. Besides some minor data gaps in this continuous operation, there is a large period with no data return between sols 267–288. This is due to the solar conjunction period where Earth-Mars communications were obscured by the sun as consequence of their relative orbital positions. With respect to the Local Mean Solar Time (LMST, local InSight time, e.g. Allison & McEwen, 2000), the polarization patterns prevail over many sols and we discuss some of them in the following to understand the glitch behaviour in more detail. First, we demonstrate that our polarization analysis is correct and explain why the results are not intuitive for certain cases for VBB and SP. We then discuss glitches occurring on only one VBB or SP component before building our arguments for multi-component glitches. We conclude this section by looking at glitches that occurred simultaneously on VBB and SP. Note that all details concerning the SEIS sensor assembly and available SEIS channels can be found in Lognonné et al. (2019).

3.1 Theoretical Considerations for apparent Glitch Polarizations

The glitch polarization describes the direction (azimuth and inclination) in which the SEIS sensor assembly is accelerated in order to produce the observed glitch signal on the three sensors U, V and W of VBB and SP, respectively. Thus, irrespective of analyzing a one-component or a multi-component glitch, we map the non-orthogonal UVW-components (Fig. 1a,c) into the orthogonal ZNE-components before computing azimuth and inclination. For a one-component glitch the non-orthogonality of the VBB components leads to the non-intuitive result in that the azimuth differs slightly from the azimuth of the affected sensor while the incidence angle of the same one-component glitch differs by $\sim 12°$ from the sensor's dip angle. We demonstrate this relation in the following.

Projecting the seismometer components from the orthogonal basis vectors Z (positive up), N (positive North), and E (positive East) onto the arbitrarily oriented basis of UVW, we must start with the following linear system of equations:

$$\begin{pmatrix} U \\ V \\ W \end{pmatrix} = \underbrace{\begin{pmatrix} -\sin(\delta_U) & \cos(\delta_U)\cos(\phi_U) & \cos(\delta_U)\sin(\phi_U) \\ -\sin(\delta_V) & \cos(\delta_V)\cos(\phi_V) & \cos(\delta_V)\sin(\phi_V) \\ -\sin(\delta_W) & \cos(\delta_W)\cos(\phi_W) & \cos(\delta_W)\sin(\phi_W) \end{pmatrix}}_{A} \cdot \begin{pmatrix} Z \\ N \\ E \end{pmatrix}, \tag{1}$$

where A represents the base transformation matrix, δ_i the sensor dip of sensor i, and ϕ_i the sensor azimuth of sensor i clockwise from N. Note that sensor dips are defined as positive downwards from the horizontal plane (e.g. Ahern et al., 2012). To reconstruct data recorded in the UVW-system into the ZNE-system, we must use the inverse operation:

$$\begin{pmatrix} Z \\ N \\ E \end{pmatrix} = A^{-1} \cdot \begin{pmatrix} U \\ V \\ W \end{pmatrix}, \tag{2}$$

with A^{-1} the inverse matrix of A. If we now consider a glitch that occurred only on VBB U with an amplitude $U = 1$ ($V = 0, W = 0$), insert those values into Equation 2, and use the following equations to determine the apparent glitch azimuth defined clock-wise from N, AZ, and apparent glitch incidence defined from Z, INC, it follows:

$$\begin{aligned} AZ &= \text{atan2}\ (E, N) = \text{atan2}\ (A_{31}^{-1}, A_{21}^{-1}) \\ INC &= \text{acos}\left(\frac{\langle [Z,0,0]^T, [Z,N,E]^T \rangle}{\| [Z,0,0]^T \| \cdot \| [Z,N,E]^T \|}\right) = \text{acos}\left(\frac{A_{11}^{-1}}{\sqrt{(A_{11}^{-1})^2 + (A_{21}^{-1})^2 + (A_{31}^{-1})^2}}\right). \end{aligned} \tag{3}$$

We can calculate the inverse matrix elements A_{j1}^{-1} with the known VBB U sensor azimuth and dip $\phi_U = 135.1°$ and $\delta_U = -29.7°$, respectively, and find:

$$\begin{aligned} AZ &= 134.6° \neq 135.1° = \phi_U \\ INC &= 48.5° \neq 60.3° = 90.0° + \delta_U. \end{aligned} \tag{4}$$

Therefore, the apparent azimuth and incidence angles of a one-component VBB glitch will *not* point in the direction parallel to the sensitive direction of the affected VBB sensor. Instead, the vector spanned is parallel to the vector cross-product of the remaining two components that do not show the glitch. Due to the similar arrangement of all VBB's sensors, with azimuths of $\phi_U = 135.1°$, $\phi_V = 15.0°$ and $\phi_W = 255.0°$, and dips of $\delta_U = -29.7°$, $\delta_V = -29.2°$ and $\delta_U = -29.4°$ (Fig. 1a), the case demonstrated for VBB U holds true for VBB V and VBB W, too. Therefore for all VBB components, a one-component glitch polarization analysis will deliver azimuth angles (almost) parallel to the sensor azimuths and hence be intuitive, whilst incidence angles will be $INC \sim 48°/132°$ as opposed to the sensor incidences of $90.0° + \delta_i \approx 60°$ (or $120°$). For multi-component VBB glitches similar considerations disclose the calculated azimuths will also be intuitive, however, for a two-component glitch the incidence must be $INC \simeq 30.0°$–$150°$ (within a plane orthogonal to the third

component), whilst for a three-component glitch the incidence can range the whole parameter space of $INC = 0°$–$180°$. It follows immediately that any VBB glitch for which we observe an $INC < 30°$ or $INC > 150°$ must, necessarily, affect all three VBB components.

Doing the same exercise for SP, with azimuths of $\phi_U = 285.0°$, $\phi_V = 105.2°$ and $\phi_W = 345.3°$, and dips of $\delta_U = -89.9°$, $\delta_V = 0.0°$ and $\delta_U = 0.0°$ (Fig. 1c), one finds that for SP U (Z) the azimuth and incidence angles will follow one's intuition closely and be 0° and 0°, respectively. For the horizontal components SP V and SP W the case is different: a SP V glitch will reveal an incidence angle of $INC = 89.9°$–$90.1°$ as expected, but an azimuth of $AZ \sim 075°/255°$, which is not intuitive given its sensor azimuth of $\phi_V = 105.2°$. Similarly for SP W, the incidence angle will be $INC = 89.9°$–$90.1°$ but the azimuth $AZ \sim 015°/195°$, as opposed to the sensor azimuth of $\phi_V = 345.2°$. A direct consequence is that any SP glitch pointing parallel to the SP V or SP W sensor azimuths must be in fact a multi-component SP glitch. For multi-component SP glitches, we did not detect any glitches that occur on the vertical SP U component in combination with either one or two of the horizontal components SP V and SP W. That is, the only multi-component SP glitches are two-component glitches on SP V and SP W. Multi-component SP glitches are therefore always oriented in the horizontal plane.

The message from these theoretical considerations is that our glitch polarization analysis will deliver azimuths and incidence angles that correctly incorporate the non-orthogonality of VBB and SP; the vectors spanned by these angles point into the only physically possible directions for a given one-, two- or three-component glitch. On the other hand, for the interpretations of these angles, it must be born in mind that VBB incidence angles may carry counter-intuitive information, whilst SP azimuth angles for one-component glitches will not align with the respective sensor azimuths but diverge by $\sim 30°$. We have started this section by stating that the glitch polarisation points in the direction in which SEIS has to be accelerated in order to produce the observed output. However, for glitches which are not associated with an acceleration of the entire sensor assembly (i.e. no tilt of the whole SEIS instrument) the adopted convention needs to be used with caution - particularly given the non-orthogonality of the sensors. Still we feel that the concept of glitch polarization is useful.

At this stage we also note that whilst the poles and zeros of the seismometer responses are well determined, the same does not apply fully for the generator constants (gains). In the worst case they may differ up to 10% from the absolute values known by pre-mission tests. To convince ourselves of the correctness of determined glitch azimuths and incidences with respect to these constants we conducted a test: we took the raw data of one- and multi-component glitches of different amplitudes and divided the respective components by their gains that we allowed to vary each by up to ±10%. For each permutation, we then rotated into the ZNE-system and performed the polarization analysis. For VBB, we find that glitch azimuths and incidences generally stay within ±5° and ±4°, respectively. For SP, we find that glitch azimuths and incidences generally stay within ±3° and ±1°, respectively, the latter of which is because SP multi-component glitches occur only on the horizontal components. All these values are smaller than the typical errors of polarization measurements and we can therefore assume the resulting glitch patterns to be reliable.

3.2 Glitches on only one seismometer component

For VBB, amplitudes of one-component glitches are usually $<1e^{-7}ms^{-1}$ and are thus not amongst the largest ones observed. Furthermore, a glitch occurring on only one single component cannot be interpreted as the SEIS instrument tilting. Such a glitch would necessarily have an incidence angle of $INC \sim 48°/132°$ (see Section 3.1) whilst the only possible direction of acceleration change would point (nearly) in the horizontal plane for a true SEIS tilt. We hence conclude that VBB one-component glitches can only be related to instrumental artifacts such as (but not limited to) thermally driven stress relaxations in the suspension spring or pivot, displacement of one of the fixed plates of the displacement transducer, voltage offsets in the individual feedback electronics, or tilting of the individual sensor within the SEIS frame. Figure 3a,b shows the VBB one-component glitches. For most identifiable patterns we find their behaviour clearly changed either when the SEIS heaters were turned on (these are mounted on the leveling ring, see Lognonné et al., 2019) on Sol 168 (2019-05-19), or after the solar conjunction period in which the heaters were off and the SEIS instrument cooled down. This plus the fact these glitch patterns emerge due to their recurrence with respect to the local time, i.e. repetitively at the same time of the sol, leads us to conclude that they are indeed thermally driven. What we suspect is that the enormous Martian surface temperature changes, that

can reach up 100°C each sol, introduce stresses into the material – possibly within the Evacuated Container. Even though the temperatures inside SEIS do not vary as much as outside, the stresses grow and are released once at a critical temperature is reached, thereby producing a glitch. When the heaters are on, the SEIS' thermal regime exhibits essentially higher temperatures and, in second order, lower diurnal amplitudes and thermal spatial gradients. This contributes to minimize thermal stresses in this complex assembly, thus diminishing or at least altering glitch production. We demonstrate heater-related glitch behaviour in more detail in the next Section 3.3 for multi-component glitches. We have no good explanation why we observe so many more glitches on VBB W compared to the other two VBB components, especially after the conjunction period during which the SEIS heaters were off. Only after ∼100 sols after the conjunction the number of one-component glitches (mostly constituted by glitches on VBB W) return to the pre-conjunction level (Fig. 3b).

For SP, a glitch occurring on only one single component could potentially be interpreted as the SEIS instrument tilting if the glitch shows one of the two horizontal components, SP V (2) or SP W (3). The tilt direction must furthermore be orthogonal to the other horizontal component so the glitch could only be seen on one component. More plausible than being caused by SEIS tilt we think is that these glitches are also thermally driven. Figure 3c demonstrates that the horizontal one-component SP glitches change their behaviour / occurrence with heater activation. For SP U, oriented almost vertically, a one-component glitch cannot be explained by instrument tilt because it does not point in the horizontal plane. These glitches therefore must relate to effects on the sensor level. Interestingly, Figure 3d demonstrates that SP U glitches that occur during the morning hours, i.e. when the environment becomes warmer, point upwards whilst during the evening/night hours, i.e. during the cooling cycle, the glitches point downwards. We interpret this behaviour as further evidence for the thermally driven nature of one-component glitches. Glitches occurring on the SP U and on the (reconstructed) VBB Z in contrast support a non-mechanical origin, possibly related to voltage offsets on the displacement transducers lines.

3.3 Glitches on multiple seismometer components

The multi-component glitches for VBB and SP are illustrated in Figure 4. Especially for VBB, for which we generally detect more glitches, clear patterns emerge over the period of 2019. We discuss five of these patterns in the following.

We observe a glitch pattern with associated acceleration change pointing towards North (blue dots, pattern 1). These three-component glitches are often accompanied by glitch precursors and occur around 1800 LMST and thus when the local temperatures start dropping. The incidence angles are $\sim 90°$ (in the horizontal plane) and hence may represent the SEIS instrument tilting. For this glitch pattern, however, we observe an additional 4.2 Hz ringing in some cases for the duration of the glitch, something not expected for an unhindered SEIS tilt. This occasional ringing could be related to other short duration data artefacts ("donks", still under investigation) we observe mostly in data with higher sampling frequencies (>20 sps). Due to the apparent temperature dependence of this pattern we currently favour the possibility that they are produced by the temperature decrease resulting in slight contractions of the tether and/or Load Shunt Assembly (LSA) – located both at azimuths $\sim 15°$ and connecting SEIS with the InSight lander. This argument is supported by the fact that the heater activation on Sol 168 (2019-05-19) seemed to have no significant effect on these glitches (Fig. 4c), bearing in mind that the heaters are located within SEIS and the LSA/tether is not. Furthermore, the largest of these VBB glitches (amplitudes larger than $1e^{-7}ms^{-1}$) are also observed on SP with agreeing glitch azimuths and incidence angles (Fig. 5) and the same 4.2 Hz ringing. It therefore could be concluded that this glitch pattern is indeed due the SEIS instrument tilting, caused by cooling effects of the tether and/or LSA that also cause the 4.2 Hz ringing. On the other hand, the glitch azimuths of pattern 1 average to $\sim 0°$ and not $\sim 15°$ where the LSA/tether are located. Also, the acceleration changes associated with these glitches point northward and hence suggest SEIS tilting southward, something difficult to reconcile with e.g. the contracting tether "pulling" SEIS. One may therefore suspect not the tether itself as possible glitch cause but instead its connection with SEIS . Interestingly, there is another glitch pattern (green dots, pattern 2) with similar features: azimuths pointing consistently south (instead of north), incidence angles of $\sim 90°$, often preceding glitch precursors, occurrence ∼1000 LMST (instead of 1800), occasional 4.2 Hz ringing during the glitch, no significant effect of heater activation on glitch amount, and the largest amongst them also

visible on SP with coinciding azimuths and incidence angles (Fig. 5). This pattern could represent the counter-part to pattern 1; in the warming cycle of the sol the glitch cause reverses.

The glitches with azimuths $\sim 240°$ occurring around 2100 LMST (pink dots, pattern 3) show clear indications of being thermally driven. These three-component glitches with accompanying glitch precursors, that are not seen on SP, appear just after SEIS heater activation whilst before they were absent. Their consistent incidence angles of $\sim 100°$ prohibit their interpretation of SEIS tilting but instead point towards a thermal effect acting on all VBB sensors. After the conjunction period, during which the heaters were off, they do not immediately reappear with the heater re-activation but only $\sim$30 sols later together with azimuths being more variable. Such conjunction-delayed behaviour (before the pre-conjunction state is reached again) it is also readily visible for other multi-component patterns during the night time (red and pinks dots at azimuths of $\sim 40°$). For these reasons, such glitch patterns are likely to represent SEIS-internal, thermal effects. This is further supported by the glitch histogram in Figure 4e that clearly shows reduced glitches for the night time just after heater activation (fewer red dots). We note that there is a similar pattern on SP at azimuths of $\sim 350°$ (red dots) that occurs at the same times as the corresponding VBB one.

Another prominent VBB multi-component glitch pattern occurs in the early sol-hours with azimuths mostly due East (yellow-orange dots, pattern 4). These three-component glitches with accompanying glitch precursors, that are not seen on SP, happen during the diurnal cooling cycle. Although there seems to be no obvious influence by the heater activation (or re-activation after conjunction), with increasing sols they occur at earlier hours. This plus the fact that their incidence angles $INC \neq 90°$ exclude a rigid tilt of the SEIS instrument lets us conclude that for this pattern, too, thermal effects are the primary glitch cause.

There is another thermally-driven glitch pattern that appears on both VBB and SP in the early morning (yellow-orange-red dots, pattern 5), which again leads to glitches on the vertical VBB component ($INC \neq 90°$). It is discussed in detail in the next Section 3.4.

Patterns 3–5 are therefore all associated with non-horizontal incidence angles suggesting that the three VBB sensors are not detecting an overall instrument tilt. Instead, each of the three VBBs detects a different tilt that consequently leads to the non-zero glitch on the vertical axis. The VBB sensors are mounted on a titanium plate inside the Evacuated Container through three mounting bolts oriented at azimuths of 105° (IF1), 225° (IF2) and 345° (IF3). So, the first one is pointing roughly due east, while the two other ones point due west and are symmetrically to one another with respect to the West. This configuration produces colder temperatures on the east side during the night than on the west side (and the opposite during the day), with larger gradients between IF1-IF2 or IF1-IF3 than between IF2-IF3. This is likely the primary source of these thermal glitch patterns. We note that the temperatures between the inside and outside of the EC are out of phase with the outside being ahead by about 7-9 hours (Pou et al., 2019).

3.4 Glitches on both VBB and SP

Figure 5 shows all glitches that occurred within ± 2 seconds on both VBB and SP. From these 638 glitches, 118 glitches reveal the same azimuths to within $\pm 10°$. Most of the glitches on VBB and SP that match in azimuth were discussed already in the previous Section 3.3 (green and blue dots, parts of patterns 1 and 2). As we pointed out, these glitches show incidence angles of $\sim 90°$ for both VBB and SP and therefore could signify the whole SEIS instrument tilting.

The most prominent glitch pattern in Figure 5 is the one at azimuths of $\sim 145°$ for VBB and $\sim 110°$ for SP (yellow-orange-red dots, pattern 5). From the beginning of SEIS' operational mode, these relatively strong glitches occurred once every morning with persistent glitch azimuths throughout 2019. Between sols 80–167, so before SEIS' heater activation, their onset times shift each sol by on average 4 Martian minutes ($\sim 2\%$ longer than SI minutes). This can be interpreted as the glitches occurring at a critical temperature during the cooling cycle that is reached earlier every sol as the Northern hemisphere (where InSight is) is entering the colder season. When the heaters were turned on, leading to SEIS being in a thermally mitigated state, the glitches continued drifting towards earlier times but now with an average rate of less than 2 minutes per sol. After the conjunction period, during which the heaters were turned off, we observe the same as for many other glitch patterns; a more diffuse signature of the glitch azimuths and incidence angles that seem to return to pre-conjunction states

only ∼100 sols later. Also, the onsets time now drift towards later times (red to yellow) each sol which interestingly coincides with the fact that the Martian solstice occurred just after the conjunction on Sol 308. For this pattern as a whole, we were able to clearly identify the critical temperature around which the glitches occur. As Figure 4d,f demonstrates, the glitch onset times strikingly follow the iso-temperature curve at $-54°$C for both VBB and SP. In addition for VBB, there are more patterns with similar behaviour for which we could find the critical temperatures; these correspond to pattern 3 (red and pink dots, Section 3.3). All this evidence once more supports the fact that most glitches are thermally caused. Note that the temperature sensor we used here is scientific temperature sensor A (SCIT A, channel 03.VKI), located at the northern, inner side of leveling support structure. The temperatures measured at this sensor can also occur elsewhere in the SEIS assembly at the same time.

4 Glitch Removal

Once a glitch, and its precursor if present, have been detected (Section 2) the waveforms are modeled as a linear combination of three constituents: (1) the glitch: the response of the seismometer to a step in acceleration, (2) the precursor: the response of the seismometer to a step in displacement and (3) the background drift: a first or second order polynomial. The two responses can be modeled from the pole and zero of their transfer function. Only the amplitudes and the precise timing of the source (which might be between two recorded samples) are to be inverted with such model.

The MPS group models a glitch waveform for each detected glitch using three parameters: an amplitude scaling factor, an offset, and a linear trend parameter. To find the best fit within a respective glitch time window, the model is iterated over each sample (no sub-sample implementation) and the best fit for the three parameters is determined. The deglitched data then is obtained by subtracting the fitted glitch without the offset and linear trend parameters from the original data. To prevent our method from removing data where the fit is not good enough, i.e. the model is fitted to data that are in fact not glitches or fitted to glitches that cannot fully be represented by our model of a step in acceleration, we correct glitches only for which we can achieve a variance reduction of $> 85\%$ with respect to the overall glitch window. We find this threshold to generally permit the removal of all large glitches whilst small glitches are also removed if their waveforms represent that of the underlying model well. This method delivers comparable results for all sampling frequencies. An example of this glitch removal is shown in Figure 6.

Two groups (ISAE and UCLA) have been carrying out glitch removal on 10/20 sps data with the UCLA group adding precursor removal, which is the approach we describe here. Glitch and precursor templates were fit to the glitches and precursors, respectively, using non-linear least squares (NLSQ). Because of the delta-like shape of the precursor over one or two sample intervals, the starting model must find the location to within a fraction of a sample interval (0.05 s). Glitches are easier to fit than precursors, being low frequency, and requirements on the starting model are less stringent. Precursors are much smaller in 2 sps data relative to glitch sizes. Thus 2 sps data were used to generate a glitch catalog (Section 2).

The starting parameters from the 2 sps fits were then used to fit glitches in the 20 sps data and residuals were calculated. The residuals were examined for the presence of a precursor in the data before the glitch peak, by requiring its amplitude to be greater than 5 standard deviations of the residuals after the peak. If true, an iterative forward model was run by shifting the phase of the precursor template about the corresponding peak in the residuals (in steps of sample interval/10), and finding the amplitude and phase of maximum cross correlation. The NLSQ was run again with both precursor and glitch templates, and the result checked whether cross-correlation of data and model are above a threshold, and if so, the results are stored. At this stage, for poly-glitches (one on top of another) we search for the precursor at the beginning of the sequence. This may need to be improved in future versions. Even though a number of precursors have been removed, there are residuals and transients that remain.

Figure 7a shows an example for glitch removal (ISAE) and glitch plus precursor removal (UCLA) from the VBB W channel for Sol 211. Atmospheric pressure effects, most notably convective vortices (Section 6.3), can also introduce signals in the seismic data. We find that transients in the time-derivative of the pressure channel (03.BDO) match, at times, closely with the glitch template. Using

the largest of these examples, we determined a transfer function, T, between the data of VBB and P. This allowed us via correlation analysis to detect whether the glitch-like signal on seismic data is caused by pressure effects and thus should not be removed from the data by deglitching.

The IPGP group inverts three consecutive sources for the glitch which allows not only to invert for multi-component glitches occurring within these 3 samples but also to invert for the phase delay through finite-difference approximation of the first and second time derivative. This linear approach allows the inversion to provide identical results in the U, V, W coordinates or in the Z, N, E coordinates, as the rotation between the two coordinates systems is a linear relation. Conversely, the three other methods, through their non-linear part of the inversion or through the cross-correlation phase fitting, have built-in small reasons to provide different solutions depending on the coordinate systems. A comparison of spectrograms before and after deglitching using this method is shown in Figure 7b,c.

In the end, all the proposed deglitching methods are nevertheless based on the same impulse response model and mostly differ by their threshold below which a glitch is removed or not. No general rule on that threshold can be provided, as it depends on the data processing target. As an example, the three methods assuming strictly a single glitch (MPS, ISAE, UCLA) and the three-point source method (IPGP) provide similar deglitching for the large glitches occurring during the cooling periods and during the night. More freedom is available for fitting longer source duration glitches during the day by the three-point sources technique, although some of the latter may represent the real response of SEIS to a small pressure drop (see Section 6.3) which can generate nano-tilts. At the same time, while many precursors are fitted by the templates, there are a significant number that have quite different morphology, longer ringing, or longer-period transient behavior. These are the subject of ongoing work.

We also point out that we have discontinued our deglitching efforts using the stationary wavelet transform as described in the Supplement V of Lognonné et al. (2020). Whilst this approach provided promising and correct results for a fair amount of cases (as far as one can tell), there is no underlying, physical model involved and the implicit data 'correction' therefore seemed too arbitrary. For many cases this approach further introduced DC-offsets in the deglitched data whose amplitudes and lengths depended on the length of data read (and therefore maximum decomposition level); an artifact that we could never manage to fully avoid.

5 Glitch Model

Throughout this paper we have assumed that glitches can be understood as steps in acceleration and glitch precursors as steps in displacement. This model allowed us to successfully detect, analyse and remove one- and multi-component glitches for both VBB and SP. In the following we detail the theoretical considerations behind this simplified model.

Let us assume glitches are caused by a small instantaneous tilt. By instantaneous we mean that the time history of the tilting is so short that it cannot be resolved with any given sampling frequency available to us (maximum 100 sps). We are thus allowed to idealize any step in time by a Heaviside function. Physically such short instantaneous events can for example be the result of stick-slip events.

The small tilt is assumed to be the result of a rotation around a horizontal axis, $\vec{a}$. Recall that the VBB is a pendulum seismometer where the (inverted) pendulum is constrained to rotate around a horizontal axis, $\vec{b}$. The sensitive direction, $\vec{s}$, of the pendulum is perpendicular to the $\vec{b}$ axis and is inclined relative to the horizontal plane by a dip angle of $\delta = -29.3°$. Let us also assume for simplicity that all the mass of the pendulum is concentrated in its center of gravity (CoG) - which would be the case for a mathematical pendulum.

Now we can distinguish five cases which differ by the location of the accelerometer relative to the tilt axis, $\vec{a}$:

(1) the two axes $\vec{a}$ and $\vec{b}$ are parallel and $\vec{a}$ passes through CoG: in this case the accelerometer gets only reoriented relative to the gravity vector but the CoG stays in place.

(2) the two axes are parallel and $\vec{a}$ does not pass through CoG but is at the same height as the CoG: in this case the accelerometer gets displaced vertically and reoriented relative to the gravity vector. However this reorientation is negligible because it is only a second order effect.

(3) the two axes are parallel and $\vec{a}$ does not pass through CoG. Furthermore a line parallel to $\vec{s}$ passing through CG intersects with $\vec{a}$. In this case the accelerometer gets displaced vertically and reoriented. However the displacement is in the direction perpendicular to the sensitive axis and hence is not seen by the accelerometer. Only the reorientation is sensed.

(4) For all other locations of the rotation axis $\vec{a}$ for which $\vec{a}$ and $\vec{b}$ are parallel the accelerometer will see both a displacement and a reorientation relative to the gravity vector.

(5) For the general case where $\vec{a}$ and $\vec{b}$ are not parallel the same arguments can be made but the effect sensed for a given tilt angle will always be reduced relative to the case with parallel axes $\vec{a}$ and $\vec{b}$ since the tilting is reduced.

As soon as the accelerometer gets reoriented relative to the gravity vector we expect to see the response due to a step in acceleration, because the projection of the gravity vector into the sensitive direction is changed. In those cases where the accelerometer gets displaced we expect to see the response due to a step in displacement. The five cases then only differ in the relative size of the displacement and tilting.

What do these signals look like? In Figure 6 we have plotted the response of the VBB sensors to a step in acceleration and the response to a step in displacement (red lines). To model the instrument response we take the full seed response and evaluate it with *evalresp* – a piece of software provided by the IRIS/DMC. Figure 6 also demonstrates how we can use the modelled glitch and precursors to remove them from the data.

Can these signals explain the data? As Figure 6 also demonstrates, the modeled responses have been shifted in time and scaled to match the data. The fit is excellent both for the low-frequency glitch and the high-frequency precursor. We take this as confirmation that our simple model is capable of explaining the glitch waveform with four parameters: start-time and amplitude of the step in acceleration plus the start-time and amplitude of the step in displacement. In fact we could show that the start times of the acceleration and displacement steps coincide to the millisecond – which is what our model predicts. Thus we only need three parameters: the start time and the amplitudes in displacement and acceleration. Determining the start time requires an excellent calibration of the high frequency part of the sensors transfer functions, as well as high sampling rate. While deglitching on the 20 sps data is therefore much more precise and has been done for two of the described methods, the deglitching on lower rate data, e.g. 10 sps (UCLA) or even 2 sps (IPGP) can be achieved, including for the precursor amplitude, however, with the signal-to-noise ratio reduced by the frequency ratio of the bandwidth. Fitting the precursor plus glitch with these three parameters implies determining the start time to sub-sample resolution. We provide a more mathematical description of our model for the glitch plus precursors phenomenon in the Supplementary Information 2.

6 Discussion

In the following we briefly discuss other aspects of glitches and precursors that we encountered during our investigations. This section shall therefore complement our understanding of glitches and detail some more implications.

6.1 Possibly locating SEIS-internal tilts

Our glitch model presented in Section 5 is valid for rotations of the sensor assembly as a whole (e.g. caused by a change at one foot of the sensor assembly), for just the VBB sensors (e.g. caused by stick-slip events originating at the interface between the Evacuated Container and the leveling support structure), but also for an individual sensor (e.g. caused by stick-slip events originating at the sensor-support interface or at the fixed side of the pivot or spring). Each of these cases implies a different value of r: the distance between VBB U to the sensor assembly feet at 16 or 21 cm (Fayon et al., 2018), or the distance from the sensor's center of gravity to its pivot with 2.6 cm (Lognonné et al., 2019).

We illustrate this geometry with the glitch example of Figure 6 and recall the glitch and precursor characteristics in Table 2. This glitch has a vertical component and can therefore not represent the SEIS instrument tilting as a whole. The azimuth of the glitch opposite (opposite of acceleration)

and of the precursor (displacement) are 219° and 228°, respectively. These values average 223.5°, which is quite close to one of the plate's mounting bolts IF2, located at 225°. The opposite signs of the glitch amplitudes of VBB V and VBB W suggests a deformation relatively symmetrical with respect to the IF2 azimuth, while the low amplitude glitch on VBB U suggests the latter to be much reduced between the two other IFs. This glitch is therefore compatible with a radial deformation of the mounting bolts IF2. Further analysis on the impact of the thermo-elastic stresses in the VBB sphere and the resultant glitch generation will however be demonstrated in a future publication.

Table 2. Night time glitch example from Figure 6: calculated precursor amplitudes and resulting geometry parameters.

Component	Glitch amplitude (nm/s^2)	Precursor amplitude (nm)	Tilt (nrad)	Apparent radius r (m)
U	1.48	0.58	-0.46	-1.270
V	179.37	-2.44	-55.4	0.044
W	-258.7	3.03	80.0	0.038

During the night, very small but also large rotation radii are found, likely resulting from internal deformation of the Evacuated Container triggered by thermal effects, as discussed previously. During the day however, the rotation radii of the glitches are more stable and in the range 10–30 cm, suggesting an external source and therefore rigid tilt of SEIS, likely generated by the atmospheric activity.

6.2 Loading with Arm

The InSight mission includes the Heatflow and Physical Properties Probe (HP^3, Spohn et al., 2018) that includes a probe (the "mole") intended to hammer itself 3–5 m into the regolith. The mole has had difficulty getting started, and so the lander's Instrument Deployment Arm (IDA) has been pressed into service to help. On several occasions, the IDA has pushed down on either the regolith or the mole itself. When the IDA pushes down, it induces an elastic response in the regolith, deforming the surface into a funnel shape, inducing a tilt at the seismometer about 1.2 m away. This tilt of about 70 nrad is clearly observable on both the SP and VBB sensors in Figure 8 as steps in the horizontal accelerations.

In this example, at the start of the command sequence the IDA was pushing down lightly on the mole, and was given four commands: 1) move up to get off the mole, 2) move down to just above the mole, and 3) move down to reload the mole with a downward force.

We see in the seismometer data the first move up and the resulting tilt up to the NE. The arm resonates after it loses contact with the mole, and we see that as the 4 Hz ringing in the seismometer data. The seismometer does not have a significant response to the horizontal move. Then on the second move, it appears that the IDA actually touched the mole while stopping and then rebounded and resonated while hovering in mid-air just above the mole. Finally the IDA moves down to load the mole and we see a tilt down to the NE at the seismometer.

We also see several glitches that happen at the same time as the IDA motions. One of the tell-tale signs of a glitch is when we observe an offset in acceleration in the vertical component. Another indication of a glitch in this case is that the BHE-component shows steps of the same sign for both the unloading and loading. Two of the glitches appear to involve the whole sensor assembly as they are seen on both the VBB and SP. Other glitches seem to be limited to one or more components of the VBB.

6.3 Atmospheric Pressure

Pressure effects such as convective vortices ("pressure drops" or "dust devils", e.g. Lorenz et al., 2015; Kenda et al., 2017, turbulence in the atmospheric planetary boundary layer (Murdoch et al., 2017; Banfield et al., 2020), gravity waves (Spiga et al., 2018; Garcia et al., 2020) and acoustic waves (Martire et al., under review in this issue) are generating signals on SEIS components from 0.5 mHz

up to about 2 Hz. Among these pressure related perturbations, convective vortices are generating the largest physical signals observed on SEIS. Their dominant period, as observed by SEIS, can be close to the one of the glitches depending on their size, distance to SEIS and wind speed (Murdoch et al., under review in this issue). These strong signals are observed on horizontal SEIS components due to effects like ground tilt and therefore are good candidates to be detected as glitches.

7 Conclusions

We have developed a possible physical model for the generation of glitches and their associated high-frequency precursors that occur simultaneously with the glitch onsets. In this model, glitches represent steps in the acceleration sensed by the individual sensors convolved with the instrument responses whilst glitch precursors represent steps in the displacement sensed by the individual sensors convolved with the instrument responses. We used our model to develop different algorithms for the glitch detection that are all able to identify most of the high amplitude glitches for both the VBB and SP seismometers (Section 2, Fig. 2). Based on the model we furthermore demonstrate that most glitches are thermally-driven (Section 3, Figs. 3–5). Such glitches likely represent SEIS-internal tilts that differ for the individual sensors and hence produce glitches on the vertical components, an observation that cannot be reconciled with the whole SEIS instrument physically tilting. Only a small fraction of all observed glitches can be explained by a tilt of the SEIS package. We illustrate the two cases of most common glitch production in Figure 9. Other types of glitches can be caused by convective vortices or movements of Insight's robotic arm (Fig. 8). The removal of glitches and precursors, based on our model, has proven successful in many cases for both seismometers (Section 4, Figs. 6–7). Of course, there remain glitches and precursors especially of smaller amplitudes that we can not sufficiently well fit and therefore confidently remove. Nevertheless, our approach has proven beneficial and users of InSight's seismic data should therefore profit from deglitching the data following our considerations presented in this study.

As no glitch removal algorithm can warrant a perfect clean-up of all glitches and their precursors, we decided to not provide a deglitched time series of all available data. Instead, we have assembled our algorithms for glitch detection (Section 2), glitch polarization analysis (Section 3) and glitch removal (Section 4) into one Python / ObsPy toolbox. The package also holds MATLAB scripts to perform glitch detection and removal tasks as presented. Its link is: `https://pss-gitlab.math.univ-paris-diderot.fr/data-processing-wg/seisglitch`. Documentation is available. Together with this code we also provide deglitched data for a selection of seismic events.

Acknowledgments

We acknowledge NASA, CNES, partner agencies and Institutions (UKSA, SSO, DLR, JPL, IPGP-CNRS, ETHZ, IC, MPS-MPG) and the operators of JPL, SISMOC, MSDS, IRIS-DMC and PDS for providing SEED SEIS data: `http://dx.doi.org/10.18715/SEIS.INSIGHT.XB\_2016`. French teams acknowledge support from CNES as well as Agence Nationale de la Recherche (ANR-14-CE36-0012-02 and ANR-19-CE31-0008-08). The Swiss contribution in implementation of the SEIS electronics was made possible through funding from the federal Swiss Space Office (SSO), the contractual and technical support of the ESA-PRODEX office. The MPS-MPG SEIS team acknowledges funding for development of the SEIS leveling system by the DLR German Space Agency. FN acknowledges partial support from the InSight PSP program under grant 80NSSC18K1627. Documentation is available. This paper is InSight Contribution Number 128.

References

Ahern, T. K., Buland, R., Halbert, S., Styles, Ray, Skjellerup, Kris, Casey, Rob, ... Trabant, Chab (2012). *SEED Reference Manual.* IRIS.

Allison, M., & McEwen, M. (2000). A post-pathfinder evaluation of areocentric solar coordinates with improved timing recipes for mars seasonal/diurnal climate studies. *Planetary and Space Science*, *48*(2), 215 - 235. Retrieved from `http://www.sciencedirect.com/science/article/pii/S0032063399000926` doi: https://doi.org/10.1016/S0032-0633(99)00092-6

Banerdt, W. B., Smrekar, S. E., Banfield, D., Giardini, D., Golombek, M., Johnson, C. L., ... Wieczorek, M. (2020, February). Initial results from the InSight mission on Mars. *Nature Geoscience*. doi: 10.1038/s41561-020-0544-y

Banfield, D., Spiga, A., Newman, C., Forget, F., Lemmon, M., Lorenz, R., ... Banerdt, W. B. (2020, February). The atmosphere of Mars as observed by InSight. *Nature Geoscience*. doi: 10.1038/s41561-020-0534-0

Beyreuther, M., Barsch, R., Krischer, L., Megies, T., Behr, Y., & Wassermann, J. (2010, May). ObsPy: A Python Toolbox for Seismology. *Seismological Research Letters*, *81*(3), 530–533. doi: 10.1785/gssrl.81.3.530

Clinton, J., Giardini, D., Böse, M., Ceylan, S., van Driel, M., Euchner, F., ... Teanby, N. A. (2018, December). The Marsquake Service: Securing Daily Analysis of SEIS Data and Building the Martian Seismicity Catalogue for InSight. *Space Science Reviews*, *214*(8), 133. doi: 10.1007/s11214-018-0567-5

Fayon, L., Knapmeyer-Endrun, B., Lognonné, P., Bierwirth, M., Kramer, A., Delage, P., ... Banerdt, W. B. (2018, December). A Numerical Model of the SEIS Leveling System Transfer Matrix and Resonances: Application to SEIS Rotational Seismology and Dynamic Ground Interaction. *Space Science Reviews*, *214*(8). doi: 10.1007/s11214-018-0555-9

Garcia, R. F., Kenda, B., Kawamura, T., Spiga, A., Murdoch, N., Lognonné, P. H., ... Banerdt, W. B. (2020). Pressure Effects on the SEIS-InSight Instrument, Improvement of Seismic Records, and Characterization of Long Period Atmospheric Waves From Ground Displacements. *Journal of Geophysical Research: Planets*, e2019JE006278. doi: 10.1029/2019JE006278

Giardini, D., Lognonné, P., Banerdt, W. B., Pike, W. T., Christensen, U., Ceylan, S., ... Yana, C. (2020, February). The seismicity of Mars. *Nature Geoscience*. doi: 10.1038/s41561-020-0539-8

InSight Mars SEIS Data Service. (2019). *SEIS Raw Data, Insight Mission.* IPGP, JPL, CNES, ETHZ, ICL, MPS, ISAE-Supaero, LPG, MFSC. doi: https://doi.org/10.18715/SEIS.INSIGHT.XB_2016

InSight Marsquake Service. (2020). *Mars seismic catalogue, insight mission; v2 2020-04-01.* ETHZ, IPGP, JPL, ICL, ISAE-Supaero, MPS, Univ. Bristol. Retrieved from `http://www.insight.ethz.ch/seismicity/catalog/v2` doi: 10.12686/a7

Kenda, B., Lognonné, P., Spiga, A., Kawamura, T., Kedar, S., Banerdt, W. B., ... Golombek, M. (2017, October). Modeling of Ground Deformation and Shallow Surface Waves Generated by Martian Dust Devils and Perspectives for Near-Surface Structure Inversion. *Space Science Reviews*, *211*(1-4), 501–524. doi: 10.1007/s11214-017-0378-0

Krischer, L., Megies, T., Barsch, R., Beyreuther, M., Lecocq, T., Caudron, C., & Wassermann, J. (2015, May). ObsPy: A bridge for seismology into the scientific Python ecosystem. *Computational Science & Discovery*, *8*(1), 014003. doi: 10.1088/1749-4699/8/1/014003

Lagrange, J.-L. (1813). *Theorie des fonctions analytiques. nouvelle edition revue et augmentee par l'auteur.* Veuve Coucier.

Lognonné, P., Banerdt, W. B., Giardini, D., Pike, W. T., Christensen, U., Laudet, P., ... Wookey, J. (2019, January). SEIS: Insight's Seismic Experiment for Internal Structure of Mars. *Space Science Reviews*, *215*(1). doi: 10.1007/s11214-018-0574-6

Lognonné, P., Banerdt, W. B., Pike, W. T., Giardini, D., Christensen, U., Garcia, R. F., ... Zweifel, P. (2020, February). Constraints on the shallow elastic and anelastic structure of Mars from InSight seismic data. *Nature Geoscience*. doi: 10.1038/s41561-020-0536-y

Lorenz, R. D., Kedar, S., Murdoch, N., Lognonné, P., Kawamura, T., Mimoun, D., & Bruce Banerdt, W. (2015, December). Seismometer Detection of Dust Devil Vortices by Ground Tilt. *The Bulletin of the Seismological Society of America*, *105*, 3015-3023. doi: 10.1785/0120150133

Martire, G. R. F., Léo, Rolland, L., Spiga, A., Lognonné, P. H., Banfield, D., & Banerdt, W. B. (under review in this issue). Martian infrasound: numerical modeling and analysis of InSight's data. *Journal of Geophysical Research: Planets*.

Murdoch, N., Kenda, B., Kawamura, T., Spiga, A., Lognonné, P., Mimoun, D., & Banerdt, W. B. (2017, October). Estimations of the Seismic Pressure Noise on Mars Determined from Large Eddy Simulations and Demonstration of Pressure Decorrelation Techniques for the Insight Mission. *Space Science Reviews*, *211*, 457-483. doi: 10.1007/s11214-017-0343-y

Murdoch, N., Spiga, A., Lorenz, R., Garcia, R., Perrin, C., Widmer-Schnidrig, R., ... Banerdt, W. (under review in this issue). Constraining Martian regolith parameters and vortex trajectories from combined seismic and meteorological measurements. *Journal of Geophysical Research: Planets*.

Pou, L., Mimoun, D., Lognonne, P., Garcia, R. F., Karatekin, O., Nonon-Latapie, M., & Llorca-Cejudo, R. (2019, February). High Precision SEIS Calibration for the InSight Mission and Its Applications. *Space Science Reviews*, *215*(1), 6. doi: 10.1007/s11214-018-0561-y

Rossum, G. (1995). *Python Reference Manual* (Tech. Rep.). Amsterdam, The Netherlands: CWI (Centre for Mathematics and Computer Science).

Scholz, J.-R., Barruol, G., Fontaine, F. R., Sigloch, K., Crawford, W., & Deen, M. (2017). Orienting Ocean-Bottom Seismometers from P-wave and Rayleigh wave polarisations. *Geophysical Journal International*, *208*(3), 1277–1289. doi: 10.1093/gji/ggw426

Spiga, A., Banfield, D., Teanby, N. A., Forget, F., Lucas, A., Kenda, B., ... Banerdt, W. B. (2018, October). Atmospheric Science with InSight. *Space Science Reviews*, *214*(7). doi: 10.1007/s11214-018-0543-0

Spohn, T., Grott, M., Smrekar, S. E., Knollenberg, J., Hudson, T. L., Krause, C., ... Banerdt, W. B. (2018, August). The Heat Flow and Physical Properties Package (HP3) for the InSight Mission. *Space Science Reviews*, *214*(5). doi: 10.1007/s11214-018-0531-4

790 # Figures

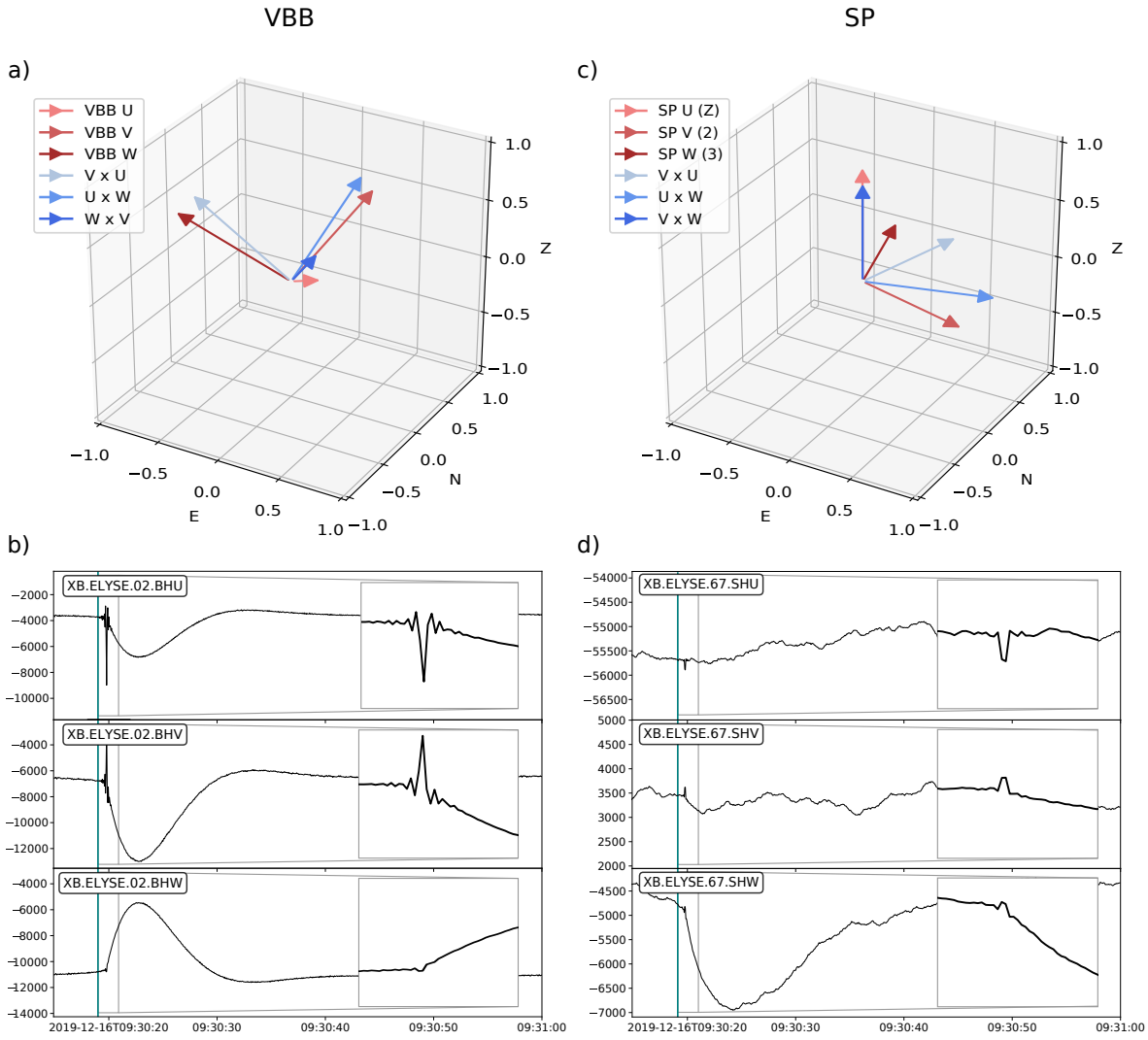

Figure 1. Sensitive directions (red arrows) of the two three-component seismometers that are part of the SEIS package; a) VBB, c) SP. Blue vectors are the pairwise vector cross-products of the sensitive sensor directions for the VBBs and SPs, respectively, and represent hence the only directions possible for the acceleration associated to one-component glitches (Section 3.1 for details and values of sensor orientations). Multi-component glitch example at 2019-12-16T09:30:19 (Sol 374) occurring on both b) VBB, and d) SP. Green lines refer to detected glitch onset after deconvolution method (Section 2.1). Note there is no glitch visible on SP U and SP V. The glitch precursors (inlays) are visible on all six seismic components, however much less on SP.

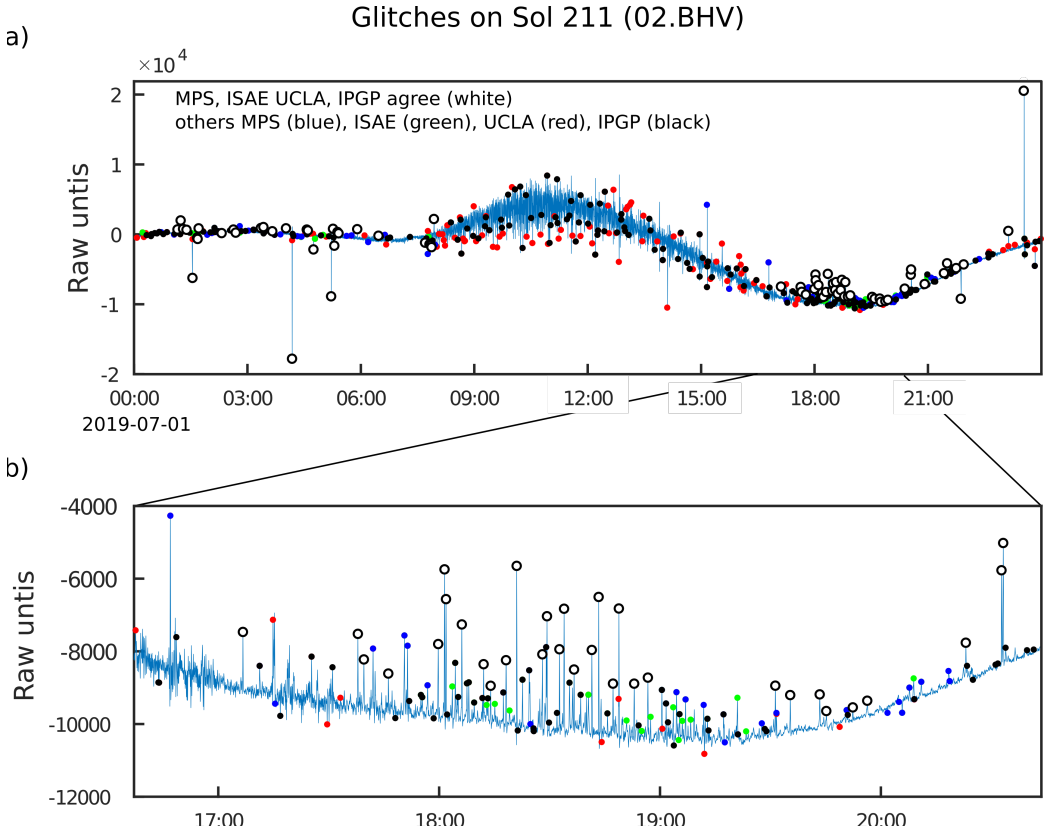

Figure 2. a) Comparison between glitches detected on 02.BHV (VBB) on July 1 2019 (Sol 211) by our four sub-groups: MPS, ISAE, IPGP, and UCLA. White circles are common glitches for all groups. Color coded symbols correspond to glitches for the different groups that are not common to all. Those common to sub-groups are plotted on top of each other and so the last plotted is shown. b) Zoomed-in section showing that as the threshold for declaring a glitch, either in terms of signal-to-noise or correlation with the template, is lowered. Results differ markedly, and some possible candidate glitches may have been missed.

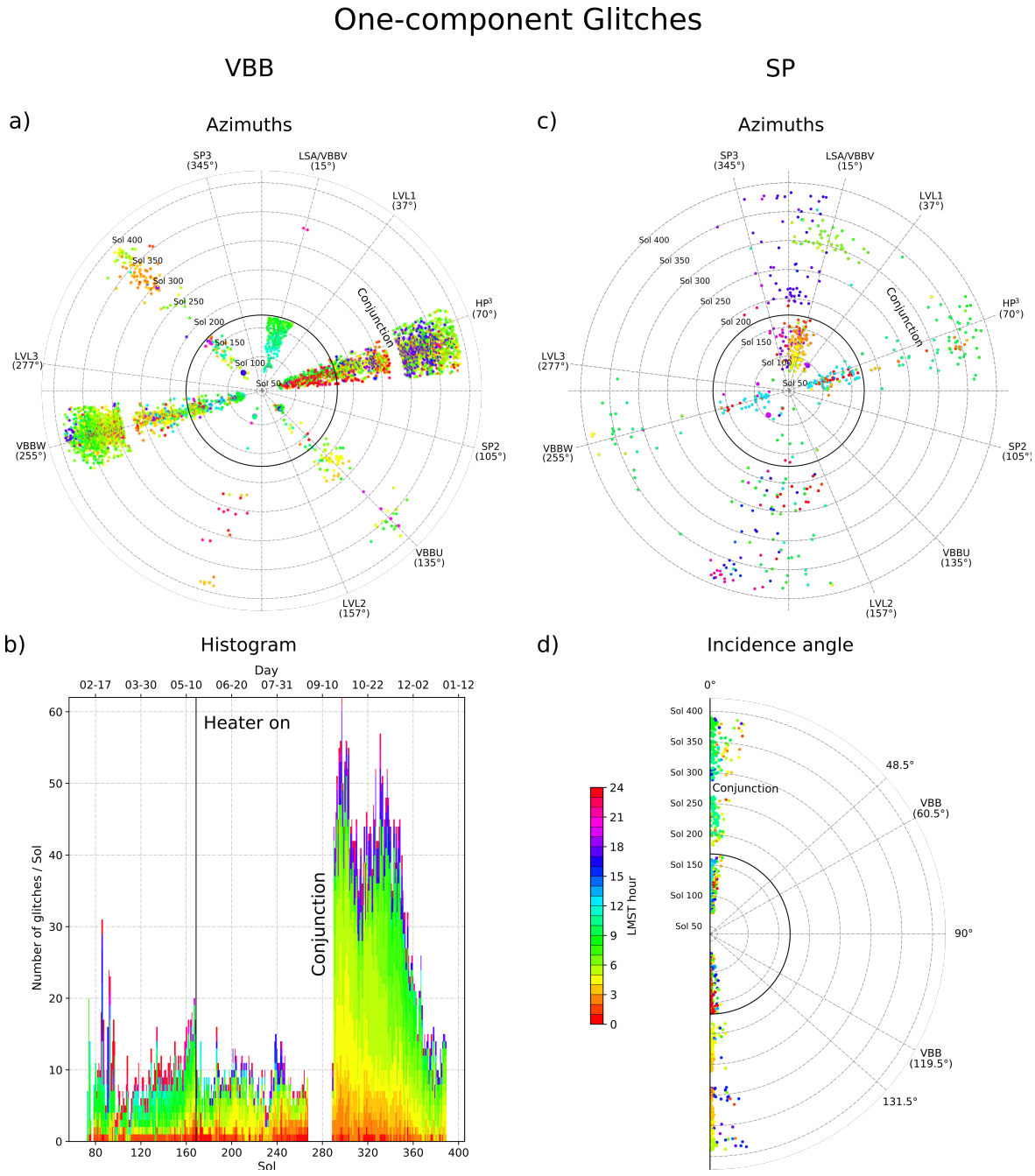

Figure 3. One-component glitches of VBB and SP for 2019 as detected by our MPS detection algorithm: a) VBB one-component glitches. Glitch azimuths align with azimuths VBB components, incidence angles are as expected $INC \sim 48^\circ/132^\circ$ (latter not shown, Section 3.2 for details), b) histogram of a). Note the rate change of glitches after heater activation (Sol 168) and conjunction (Sols 267–288), the latter mostly caused by VBB W, c) SP one-component glitches for the horizontal components SP V and SP W, and d) one-component glitches for the (almost) vertical SP U component. Color code refers to local mean solar time (LMST, in hours) of glitch onsets.

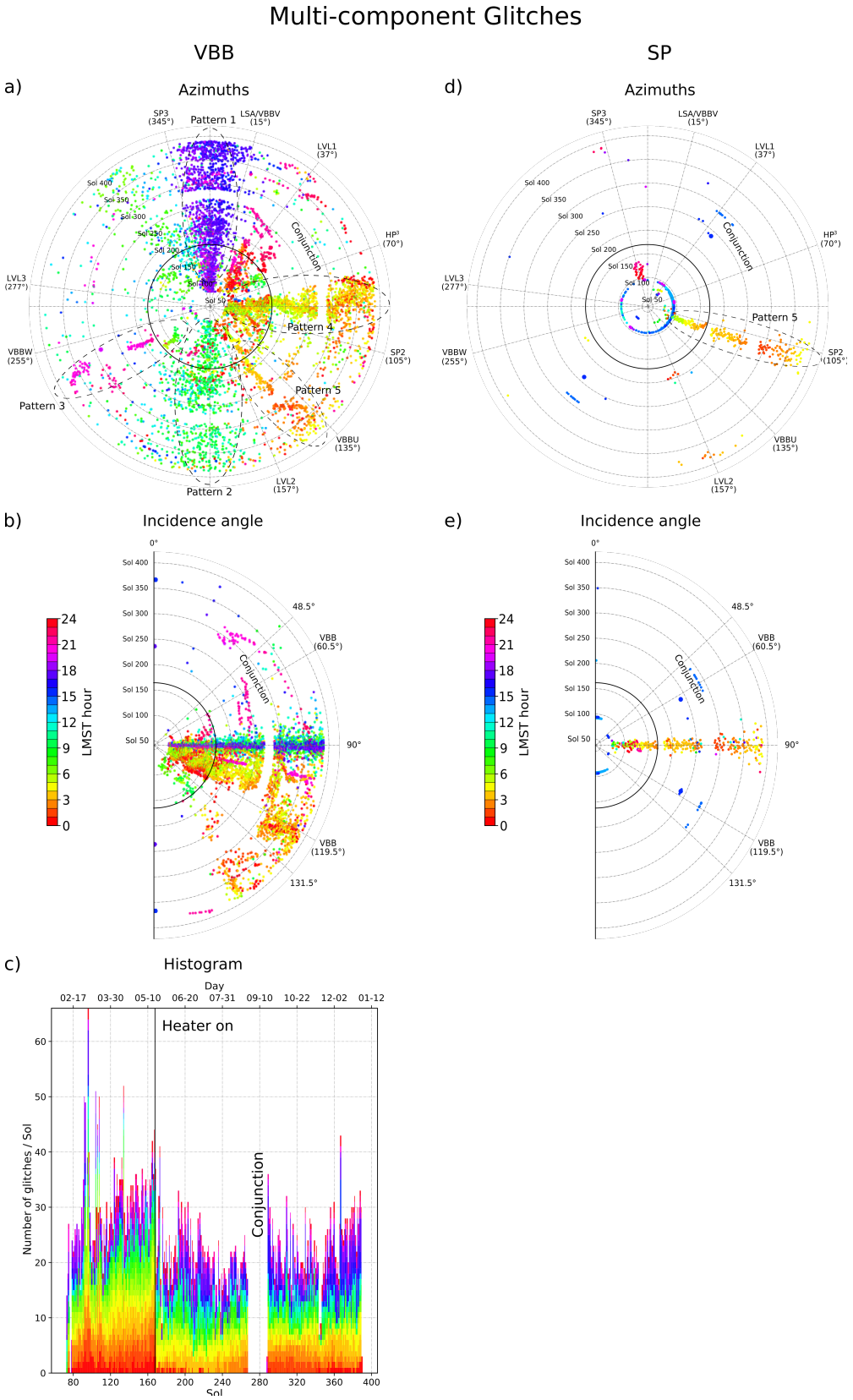

Figure 4. Multi-component glitches of VBB and SP for 2019 as detected by our MPS detection algorithm: a) VBB glitch azimuths. Marked are the five most prominent patterns (Section 3.3 for details), b) VBB glitch incidence angles point only for patterns 1 and 2 into the horizontal plane, c) histogram of a) and b). Note the rate change of night time glitches (red colors) after heater activation (Sol 168), d) SP glitch azimuths. Pattern 5, that also occurs on VBB, is marked. The blue dots mostly refer to false glitch detections caused by HP^3-hammering sessions and InSight's robotic arm movements, e) SP glitch incidence angles, demonstrating that multi-component SP glitches occur only among the horizontal SP V and SP W components. Color code is same as in Fig. 3.

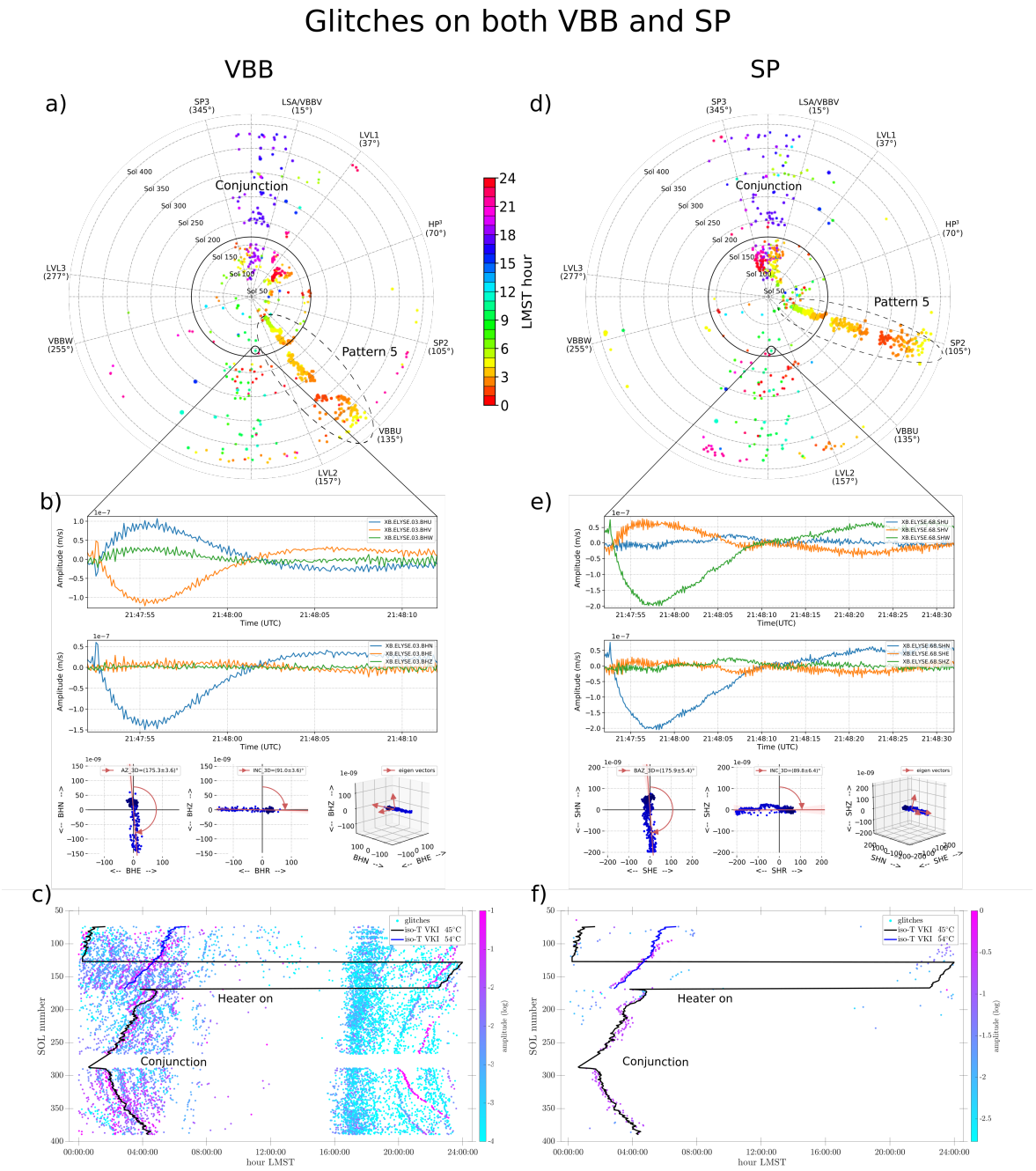

Figure 5. a,d) Glitches in 2019 that occurred simultaneously on VBB and SP. Glitch azimuths agree for patterns 1 and 2 (blue and green dots, compare Fig. 4) but not for pattern 5. Color code is same as in Fig. 3; b,e) example of our polarization analysis of the same glitch for VBB and SP on 2019-07-24T18:50:01 (Sol 234), c,f) normalised glitch amplitudes as a function of sols over hours of sol (different detection method than in sub-plots a-d). Note how the iso-temperature curve at −54°C (scientific temperature sensor A, channel 03.VKI) matches the glitches corresponding to pattern 5, thus supporting thermal causes for glitches of this pattern.

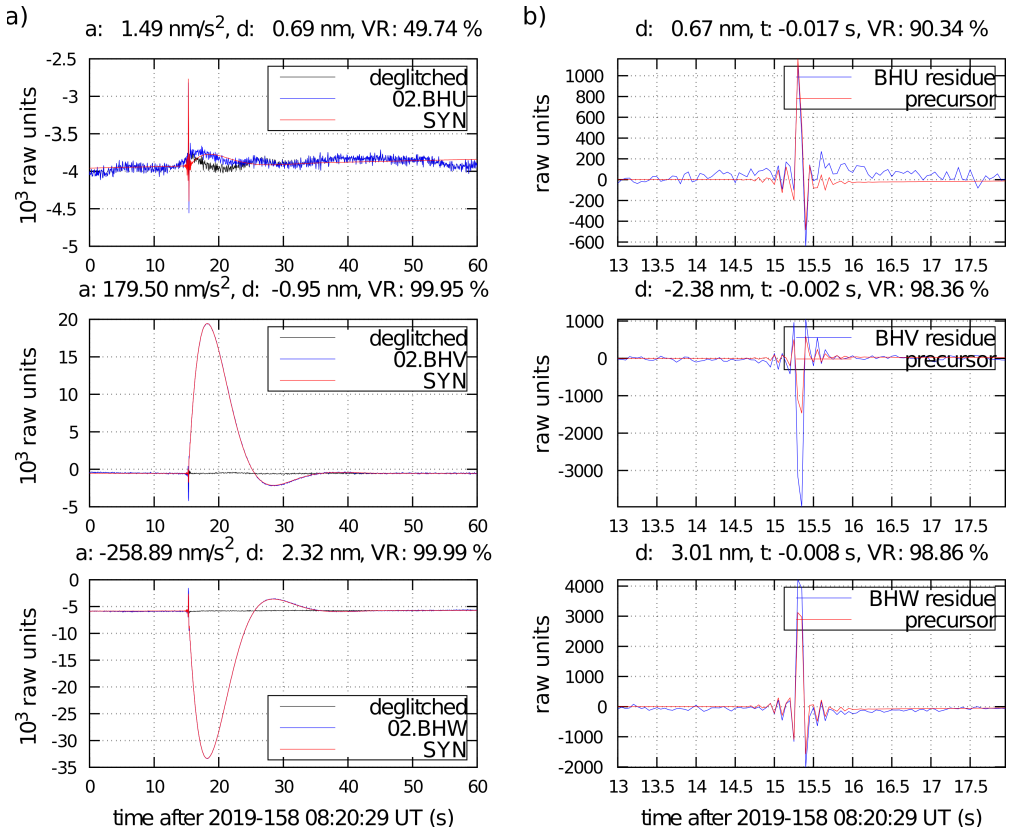

Figure 6. Automated glitch removal for VBB at work: a) we fitted the glitches (blue lines) with the nominal VBB responses to a step in acceleration (red lines). The deglitched data (black lines) were obtained by subtracting only the scaled version of the synthetic glitches from the original data, i.e. without offset and linear trend parameters. b) high-frequency precursors (red lines) were modeled with the nominal VBB responses to a step in displacement and fitted to the deglitched data of a) (blue lines). Our glitch model allows to fit both the glitch and the glitch precursors very well, even if small mismatches remain.

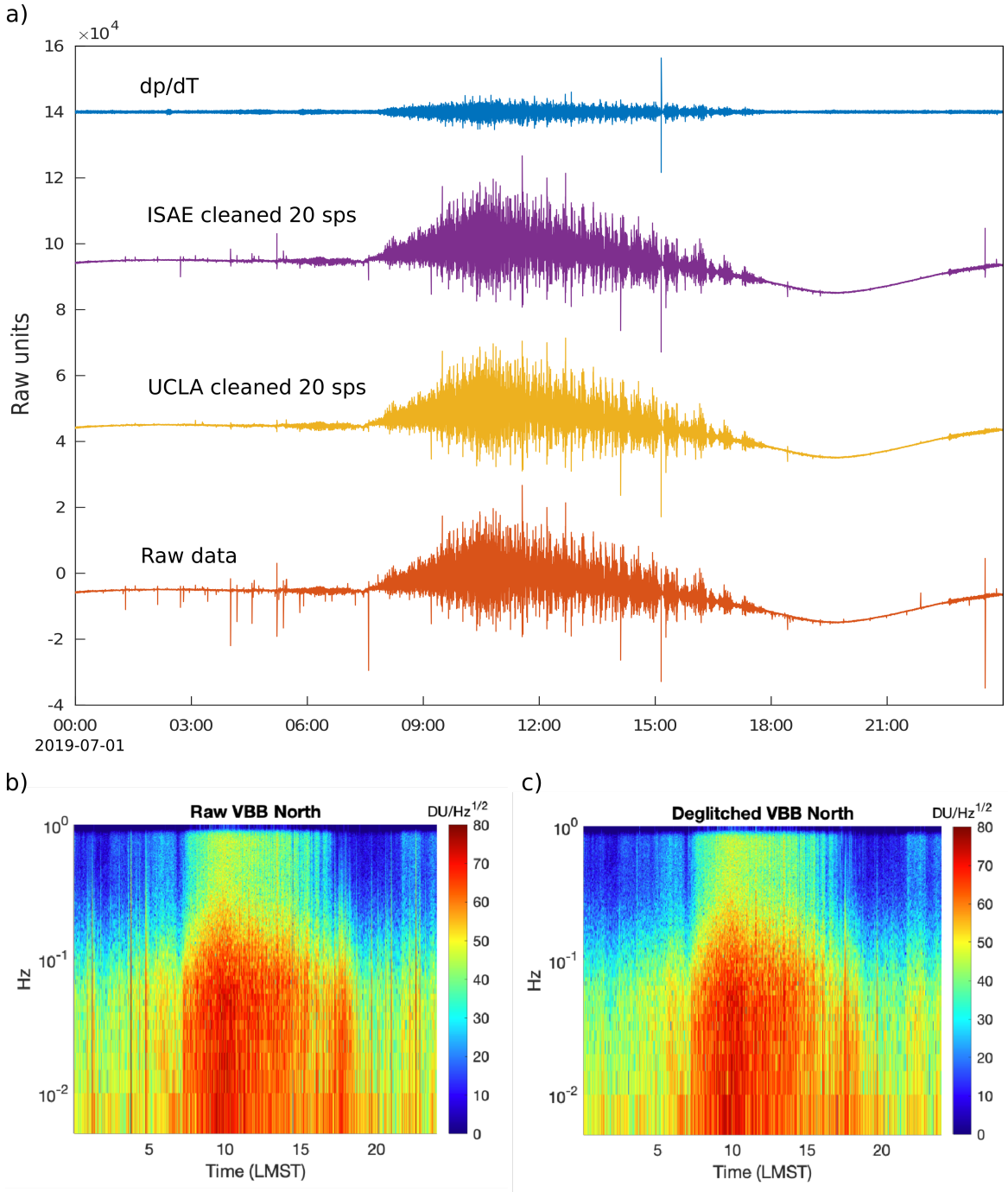

Figure 7. a) Raw time series data for 2019-07-01 (Sol 211) of the time-derivative of pressure channel 03.BDO (10 sps, blue line), VBB 02.BHW data cleaned from glitches (ISAE, purple line) and cleaned from glitches+precursors (UCLA, yellow line), and original VBB 02.BHW raw data (orange line). The large transient in the pressure data at ∼15:00 LMST survives the cleaning as has the morphology of the glitch template. A number of precursors have been removed but not all, and other transients remain that are not explained in the glitch-precursor-pressure framework, b,c) comparison of spectrograms in the 0.005–1 Hz (1–200 s) bandwidth from before (left) and after (right) deglitching using the IPGP-method: Note that the spectrograms show the VBB N-component, so the UVW data were first deglitched and then rotated to ZNE for the spectrogram calculations. With the exception of a few glitches not removed due to their significant difference with our proposed model, those removed allow a data cleaning of the down to 0.05 Hz.

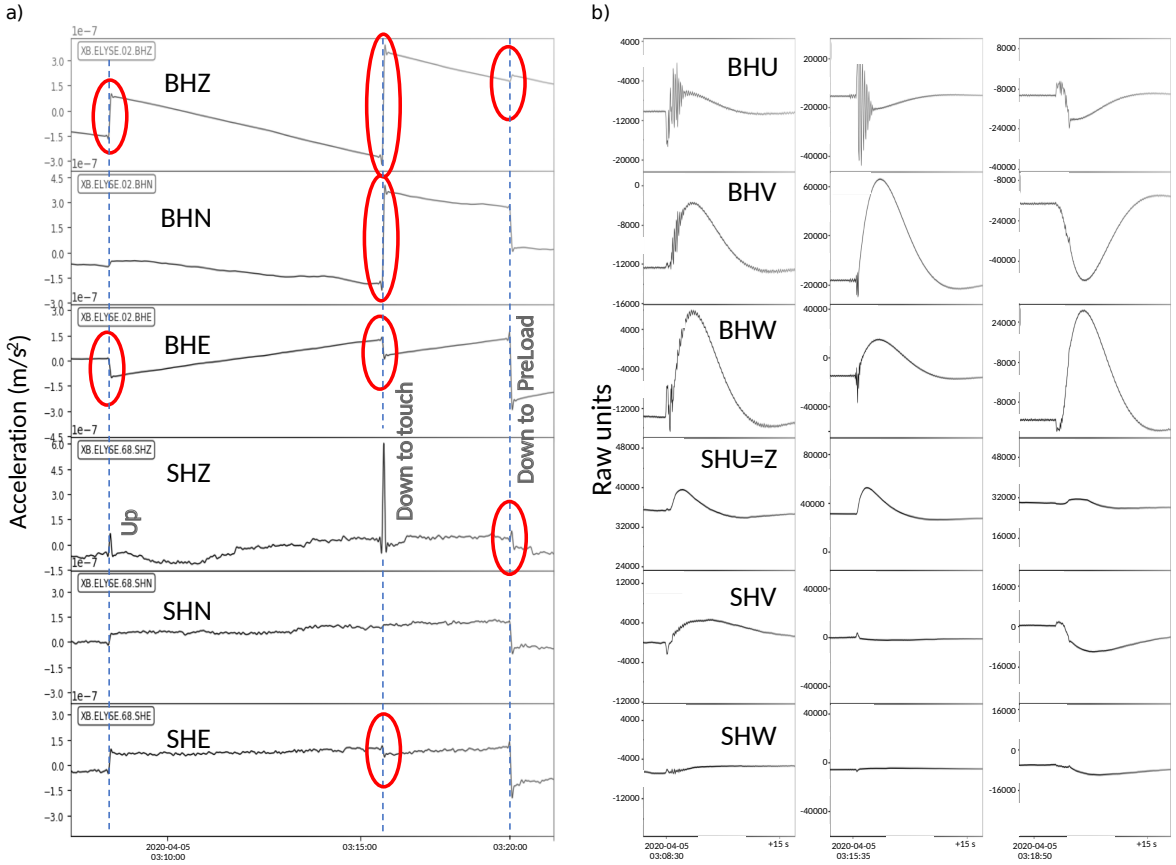

Figure 8. VBB and SP data during Instrument Deployment Arm (IDA) pushing on the HP^3-Mole. a) the arm started the sequence while pushing down on the Mole (Section 6.2 dor details). Likely glitches are identified with red ellipses in the Z, N, E plots on the left for VBB (top) and SP (bottom), b) 20 s windows of the raw U, V, W components for the arm movements indicated in a). On many of them, the canonical displacement spike followed by the tilt signature is present.

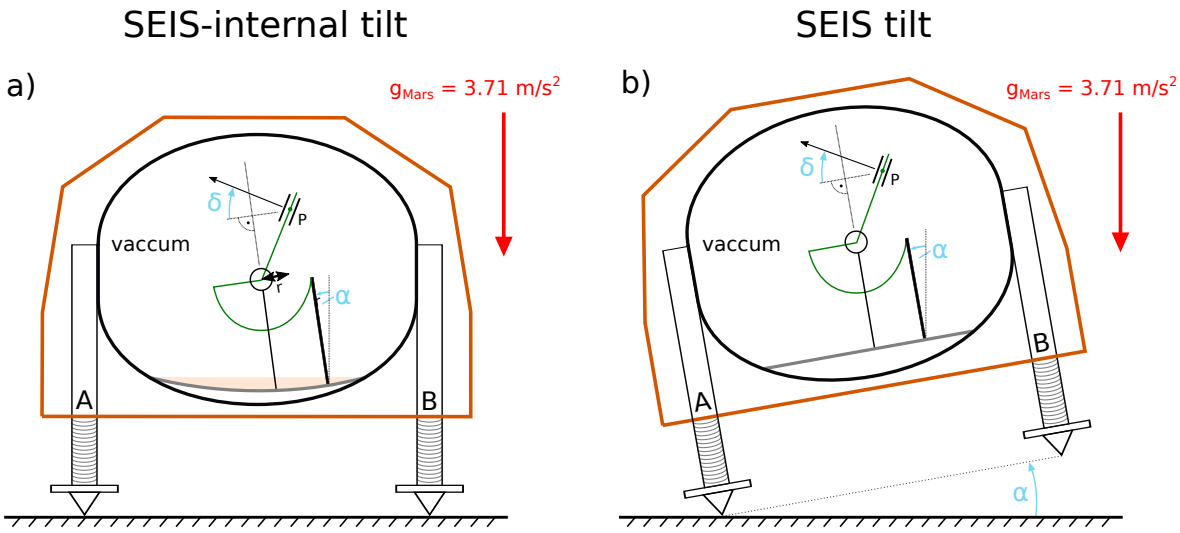

Figure 9. Simplified sketch of a cross-section through the instrument package SEIS showing only one VBB sensor: a) SEIS-internal tilt α caused e.g. by the plate that supports the VBB sensors bending (grey line and orange area). Each VBB sensor (only one illustrated) may see a different tilt, all together yielding a non-zero glitch on the (reconstructed) vertical component ($INC \neq 90^{\circ}$). We suspect such effects to be the primary reason for thermally-caused multi-component glitches such as shown in patterns 3–5 (Fig. 4). b) SEIS tilt α, corresponding to a true, rigid motion of the whole instrument. Our analysis suggests that the minority of glitches, e.g. patterns 1–2 (Fig. 4), are caused by this scenario. Note that in both cases the VBB sensors may experience a tilt and a displacement (Sections 5 and 6.1 for details). Similar considerations apply for the SP sensors that are not shown but mounted on the leveling system support structure (Fayon et al., 2018). For an accurate illustration of the SEIS sensor assembly, see Lognonné et al. (2019). P: proof mass; δ: VBB sensor dip $\sim -30^{\circ}$. The tilt α is here depicted as 10° for both cases but is in reality in the order of nano-radiant.

Supplementary Information

- SI1: Lists of glitches detected by the different methods
- SI2: Mathematical description of glitch plus precursor origins